NAVAL POSTGRADUATE SCHOOL

MONTEREY, CALIFORNIA

THESIS

A GEOMETRIC INVESTIGATION OF ACOUSTICAL WAVEFRONT SCATTERING AND HEALING INDUCED BY OCEAN INTERNAL WAVES

by

Maxsimo Salazar

March 2007

Thesis Advisor:	John A. Colosi
Second Reader:	D. Benjamin Reeder

Approved for public release; distribution is unlimited

THIS PAGE INTENTIONALLY LEFT BLANK

REPORT DOCUMENTATION PAGE		Form Approved OMB No. 0704-0188

1. AGENCY USE ONLY *(Leave blank)*	2. REPORT DATE	3. REPORT TYPE AND DATES COVERED
	March 2007	Master's Thesis

4. TITLE AND SUBTITLE A Geometric Investigation of Acoustical Wavefront Scattering and Healing Induced by Ocean Internal Waves	5. FUNDING NUMBERS
6. AUTHOR Maxsimo Salazar	
7. PERFORMING ORGANIZATION NAME(S) AND ADDRESS(ES) Naval Postgraduate School Monterey, CA 93943-5000	8. PERFORMING ORGANIZATION REPORT NUMBER
9. SPONSORING /MONITORING AGENCY NAME(S) AND ADDRESS(ES) N/A	10. SPONSORING/MONITORING AGENCY REPORT NUMBER

11. SUPPLEMENTARY NOTES The views expressed in this thesis are those of the author and do not reflect the official policy or position of the Department of Defense or the U.S. Government.

12a. DISTRIBUTION / AVAILABILITY STATEMENT	12b. DISTRIBUTION CODE
Approved for public release; distribution is unlimited.	A

13. ABSTRACT (maximum 200 words)

Observed ocean acoustic wavefronts show surprising stability in long range acoustic transmission experiments. This suggests that ocean scattering processes tend to re-distribute acoustic energy dominantly along the wavefront rather than across it. The purpose of this thesis is to elucidate the physical mechanism for this type of scattering by presenting a ray based physical model. Analytic formulae are presented that predict wavefront distortions caused by ocean internal waves and other processes. Applications of this study include wavefront healing near underwater obstacles, out of plane scattering and the vertical redistribution of energy of off axis sources.

14. SUBJECT TERMS Ocean acoustic along front scattering	15. NUMBER OF PAGES 57
	16. PRICE CODE

17. SECURITY CLASSIFICATION OF REPORT	18. SECURITY CLASSIFICATION OF THIS PAGE	19. SECURITY CLASSIFICATION OF ABSTRACT	20. LIMITATION OF ABSTRACT
Unclassified	Unclassified	Unclassified	UL

NSN 7540-01-280-5500 Standard Form 298 (Rev. 2-89)
Prescribed by ANSI Std. 239-18

THIS PAGE INTENTIONALLY LEFT BLANK

Approved for public release; distribution is unlimited

A GEOMETRIC INVESTIGATION OF ACOUSTICAL WAVEFRONT SCATTERING AND HEALING INDUCED BY OCEAN INTERNAL WAVES

Maxsimo Salazar
Lieutenant, United States Navy
B.A., Texas A&M International University, 1999

Submitted in partial fulfillment of the
requirements for the degree of

MASTER OF SCIENCE IN METEOROLOGY AND PHYSICAL OCEANOGRAPHY

from the

NAVAL POSTGRADUATE SCHOOL
March 2007

Author: Maxsimo Salazar

Approved by: John A. Colosi
Thesis Advisor

D. Benjamin Reeder
Second Reader

Mary Batteen
Chairman, Department of Oceanography

THIS PAGE INTENTIONALLY LEFT BLANK

ABSTRACT

Observed ocean acoustic wavefronts show surprising stability in long-range acoustic transmission experiments. This suggests that ocean scattering processes tend to redistribute acoustic energy dominantly along the wavefront rather than across it. The purpose of this thesis is to elucidate the physical mechanism for this type of scattering by presenting a ray-based physical model. Analytic formulae are presented that predict wavefront distortions caused by ocean internal waves and other processes. Applications of this study include wavefront healing near underwater obstacles, out-of-plane scattering and the vertical redistribution of energy of off-axis sources.

.

THIS PAGE INTENTIONALLY LEFT BLANK

TABLE OF CONTENTS

THIS PAGE INTENTIONALLY LEFT BLANK

LIST OF FIGURES

ACKNOWLEDGMENTS

I would sincerely like to thank my advisors Professor John A. Colosi and Commander D. Benjamin Reeder, Academic chair, Professor Mary Batteen, and GSEAS Program Officer Commander Denise Kruse for their unrelenting help and support throughout this process. I would also like to thank Staff Oceanographer Michael Cook whose help with programming code was key in the production of a critical result in this thesis. Finally, I give thanks to my family whose love and support made this journey possible.

THIS PAGE INTENTIONALLY LEFT BLANK

I. INTRODUCTION

Observed ocean acoustic wavefronts show surprising stability in long-range acoustic transmission experiments. This suggests that ocean scattering processes tend to redistribute acoustic energy dominantly along the wavefront rather than across it. The physical mechanism for this type of scattering has not yet been elucidated.

There are several practical implications for this type of scattering. First, scattering along the wavefront leads to the important result that shadow zones behind ocean obstacles, like seamounts, will be filled in more rapidly than by simple diffraction. Second, this type of scattering can lead to significant transfer of acoustical energy from high angles to low angles. Hence, an off-axis source, like those responsible for the ocean ambient sound fields, will have their energy redistributed vertically, thus altering the vertical directionality of the ambient sound. Thirdly, scattering along the front can contribute to the vertical extension of acoustical caustics zones that abut shadow zones. Observations reported by Dushaw et al. (1999) of the Acoustic Thermometry of Ocean Climate group on Navy SOSUS stations showed that wavefront data obtained from these stations had experienced dramatic vertical extensions of wavefront caustics several hundreds of meters above the receivers. The resultant scattering caused interference patterns along the front and vertically extended the front into shadow zones (Figure 1).

Finally, since this scattering mechanism leads to acoustical energy redistribution along the front, the scattering processes can be considered to be coherent in some regards. Thus, the scattered energy can be used effectively for signal and array processing needs, but the statistics from this type of scattering has not yet been examined in detail.

With this background information in mind, we consider a pulse emitted from a point source in the ocean sound channel. In this case, an outward propagating wavefront is formed. After traveling approximately 1,000 km, the wavefront takes on an accordion shape (Figure 2). The wavefront is composed of individual segments that are joined by cusps and each point on the wavefront is identified with a ray with a specific launch angle of the source. The wavefront is thus defined by the end points of all the rays at a specific

time after emission of the pulse. After adding small-scale heterogeneities due to internal waves, each ray will be displaced some distance from its unperturbed end point. The deviation of this ray end point can be either along the wavefront or perpendicular to the wavefront. Numerical simulations in this thesis and in other work will show that the deviation is much larger along the wavefront.

The primary purpose of this thesis is to study along the front scattering using a hierarchy of models from a simple 1-D, discrete model to a fully random ocean model. The main acoustical observable is the geometry of the acoustical wavefront, and Ray methods are used to quantify the re-distribution of ray energy along and across the front. Of principal importance is the ability to predict the ocean and acoustic variables that could most affect this type of scattering. For example, many of our simple reduced physics models predict that variance of along wavefront ray deflections scale like the cube of the propagation range, while the variance of across the front ray deflections scale linearly with range. In addition, scattering in the wavefront direction is controlled by the vertical gradients of sound speed while the scattering in the ray direction depends on the sound speed perturbation itself.

II. METHODOLOGY

Ray-based acoustic propagation models with various ocean sound speed fluctuation models were used to estimate scattering along and across the wavefront. The simplest model considered was a discrete 1-D model with small angle forward scattering. Here Snell's law was linearized and used to analytically predict the trajectory of ray paths through a series of random sound speed layers. The validity of the linear approximations was examined to determine the relative contributions of along vs. across wavefront scattering as a function of the sound speed variance, the number of layers, the width of the layers, and the wavefront angle of incidence.

The next level of complexity considered a continuous 2-D random field of sound speed perturbations obeying the (GM) internal wave spectrum. Various analytic approximations to the scattering were checked through the use of Monte-Carlo numerical ray simulations that examined the scattering physics. The simplest case modeled was ray propagation through an internal wave field that was anisotropic in depth and the horizontal direction, but homogeneous in depth. A comparison of ray simulation statistics to some simple analytic expressions was easily obtained because of the simple geometry.

The last and most complicated case involved a true ocean environment, with a sound channel, and an anisotropic and inhomogeneous internal wave field. Again, Monte-Carlo ray simulations were performed to test more complicated analytic expressions for scattering along and across the front.

A. SOUND SPEED ENVIRONMENT

In this numerical experiment, the following two dimensional sound speed field is considered:

$$c(x,z) = \bar{c}(z) + \delta c(x,z), \qquad \delta c \ll \bar{c}(z) \tag{2.1}$$

where $\delta c=\left(\frac{\partial c}{\partial z}\right)_p \zeta_{IW}$ and $\bar{c}(z)$ represent the sound speed perturbation and mean sound speed profile respectively. ζ is the internal wave displacement field and $\left(\frac{\partial c}{\partial z}\right)_p$ is the potential sound speed gradient. The mean sound speed profile can then be modeled in one of two ways. Either, it is represented by the constant c_0=1500 ms^{-1} or by the more complex Munk canonical form (Munk, 1974).

$$\bar{c}(z) = c_0\left[1+\varepsilon\left(e^{-2(z-z_a)/B} + 2(z-z_a)/B - 1\right)\right] \tag{2.2}$$

Specifically, the axial sound speed (c_0) is equal to 1500 ms^{-1}, the total water depth D=5000 m, B=1000 m, the sound channel axial depth (z_a) was set to 1000 m, and ε=0.005515.

First, the potential sound-speed gradient profile is expressed as

$$\mu(\vec{r},t) = \frac{\delta c(\vec{r},t)}{c_0} \approx \left(\frac{\alpha}{g}\right) N^2 \zeta \tag{2.3}$$

where c_0 is1500 ms^{-1}, N is the buoyancy frequency and α is a dimensionless constant related to salinity and temperature, approximately equal to 24.5.

From Flatte et al (1979), a fractional sound speed variance profile was imposed in order to understand the internal wave induced sound-speed fluctuations:

$$\left\langle \mu^2(z) \right\rangle = \left\langle \mu_0^2 \right\rangle \frac{N^3(z)}{N_{ref}^3} \tag{2.4}$$

where $\left\langle \mu_0^2 \right\rangle$=6.26 x 10^{-8}, and N_{ref} = 3 cph. However, near the surface and bottom, the profile of $\left\langle \mu^2(z) \right\rangle$ will be modified in order to accommodate the internal wave vertical mode boundary condition of zero displacement at those areas. Equation 2.4 is important because it reveals the inhomogeneities of internal wave induced sound-speed fluctuations with respect to depth. As a result of a larger buoyancy frequency in the upper ocean as opposed to a deeper one, these sound-speed fluctuations are larger in the upper regime.

The task now falls to generating the random realizations of sound speed perturbations that are induced by internal waves, where, internal waves are oscillatory geophysical wave motions resulting from the Coriolis and buoyancy forces. The change in sound-speed due to internal waves is on the order of 1 ms^{-1}, with time scales lying within the regime of the Coriolis and buoyancy periods. The length scales of internal waves are of order 100 m in the vertical and 10 km in the horizontal. Further, sound-speed fluctuations caused by internal waves are the dominant source of variability of acoustic fields in the ocean.

The Garrett-Munk internal wave spectrum is utilized using the Colosi and Brown method (1998). Internal waves can be represented as horizontally propagating vertical modes. Consequently, the internal wave displacement field ζ can be considered as the sum over all possible internal waves with vertical mode number j and wave numbers k_x and k_y.

$$\zeta_{IW}(x,y,z) = \mathrm{Re}\left[\int_{-\infty}^{\infty} dk_x \sum_{j=1}^{j_{max}} g(j,k_x) A_j(z) e^{i(k_x x - \sigma_j t)}\right] \tag{2.5}$$

where A_j is the j^{th} mode function, k_x is the horizontal wave number in the propagation plane. The amplitudes of the internal waves are complex random variables with statistics described by the GM spectrum. The buoyancy frequency profile is modeled using a canonical profile as shown below.

$$N(z) = N_s e^{-z/B} \tag{2.6}$$

Here, B is still equal to 1,000 m and the surface buoyancy frequency (N_s) is set to 5 cph. However, when the background sound speed is a constant, N_s=1cph is employed. The sum of the contributions from internal wave mode numbers up to j_{max} = 200 was chosen and internal waves with horizontal wave scales from 0.5 to 409.6 km were utilized in the generation of the random realizations of internal wave induced sound speed perturbations.

A random realization of the spectrum of μ is achieved by expressing it in terms of a mode number and horizontal wave numbers k_x and k_y. The final result is

$$G_\mu(j,k_x)=\mu_0^2\frac{N^3(z)}{N_0^3}\frac{1}{M}\frac{1}{j^2+j_*^2}\frac{2}{\pi^2}\left[\frac{k_j}{k_x^2+k_j^2}+\frac{1}{2}\frac{k_x^2}{\left(k_x^2+k_j^2\right)^{\frac{3}{2}}}\ln\left[\frac{\left(k_x^2+k_j^2\right)^{\frac{1}{2}}+k_j}{\left(k_x^2+k_j^2\right)^{\frac{1}{2}}-k_j}\right]\right] \tag{2.7}$$

where $k_j=\frac{f\pi j}{N_0 B}$. Internal waves are isotropic in the horizontal direction, but anisotropic in the vertical.

B. RAY THEORY

The evolution of the wavefront is well described by the two-dimensional ray equations (Brown et al, 2003, and Beron-Vera et al 2003). They are given by

$$\frac{dx}{dt}=c\left(1-c^2p^2\right)^{1/2},\ \frac{dz}{dt}=c^2p,\ \frac{dp}{dt}=\frac{1}{c}\frac{\partial c}{\partial z} \tag{2.8}$$

where $p=\sin\theta/c$ is the ray slowness in the z-direction. The ray equations were integrated forward in time to T_{max}=1000 km/c_0 = 666.667(s), with the intermediate times being saved in increments of 0.667 seconds. These equations were solved numerically using MATLAB.

C. NO WAVEGUIDE CASE

For the case of constant background sound speed, simulations were carried out with a source depth of 1,000 m and with an initial ray angle of zero degrees. A total of 12,000 realizations of ray propagation were computed in order to accurately calculate the necessary statistics. In this case, a periodic boundary condition was implemented in order to compensate for rapid scattering to the ocean boundaries. Figure 3 shows the ray endpoints from all the realizations at the following nominal ranges: 340, 680, and 1,000 km. A dramatic depth deviation (wavefront direction) of the end point relative to the range deviation (ray direction) is clearly evident. This figure dramatically shows the dominance of scattering along the front. The rays are also seen to be scattered into an arc instead of a straight line. The arc is formed because the rays with the largest depth deviation could not get down range as far as the rays that stayed closer to the original depth. In Figure 3, the green curve represents the parabolic fit to ray end point

distributions and the red curve shows the location of the unperturbed point source front (spherical wave). The parabolic fit is used as a mean wavefront and thus this function is subtracted off the ray endpoints to yield statistics in the wavefront and ray directions. It is clear that at 1000 km the wavefront direction deviations are on the order of tens of kilometers as opposed to the order of 10 meters of the ray direction deviations. Statistical results will be given in later sections.

D. WAVEGUIDE CASE

Implementing a source depth of 1,000 m and an initial ray launch angle of $\theta_r(0) = +7^\circ$, where the angle θ_r is with respect to the x-axis, the case of the Munk background profile with internal wave induced sound speed variations was simulated. A total of 12,000 realizations of ray propagation were modeled. Figure 4 shows the ray endpoints from all the realizations at nominal ranges of 340, 680, and 1000 km. The location of the unperturbed $+7^\circ$ ray is denoted by the green dots. Further, the unperturbed front composed of initial angles between $+0^\circ$ and $+14^\circ$ is denoted with a red line. At a range of 1000 km, deviations of the ray end points in the ray direction are of the order 10 m. Again, in the wavefront direction, the order is in kilometers, demonstrating the dominance of along wavefront deviations. Also note that the scattering in the wavefront direction is seen to be asymmetrical in the sense that the wavefront is extended more towards the longer and not the shorter ranges. Statistics will be discussed in later sections.

THIS PAGE INTENTIONALLY LEFT BLANK

III. 1-D DISCRETE CASE

The oceanographic wave propagation physics leading to distinct anisotropy in wavefront distortions is geometrically complex. To alleviate this complexity, and better understand the precise geometry involved with this problem, a plane 1-D model is first considered. Although, the model is not realistic, its simplicity allows for the analytical solutions of the trajectories of individual rays which are necessary in elucidating the aforementioned geometry.

A model consisting of a layered random sound speed medium with small angle forward scattering was considered (see Figure 5). There is an incident wave with angle θ_0 (with respect to the horizontal), in a region of sound speed c_0. The incident wave refracts via Snell's Law with angular deviation $\delta\theta_1$ into region 1 of a slab with specified width L, where Colosi and Flatte (2007) defined the sound speed as $c_1 = c_0 + \delta c_1, \delta c_1 \ll c_0$. The scattered ray then moves a distance x_1 in the horizontal, taking time t_1 to cross the slab in this region. The process continues in this manner for a specified number of N slabs.

Colosi and Flatte (2007) used Snell's Law, $\frac{\cos\theta}{c} = \text{constant}$, to express a small angular deviation when there is a small sound speed perturbation δc_j. Their results are given by

$$\delta\theta_j \cong \frac{-\mu_j}{\tan\theta_0} \tag{3.1}$$

where $\mu_j = \delta c_j / c_0$ and $\theta_j = \theta_0 + \delta\theta_j$. After the scattered ray crosses each layer, an x-deflection and a travel time result. Their resulting equations are exact relations.

$$x_j = \frac{L}{\tan(\theta_0 + \delta\theta_j)}, \qquad t_j = \frac{L}{c_j \sin(\theta_0 + \delta\theta_j)} \tag{3.2}$$

After expansion in small angles, Flatte and Colosi (2007) arrived at the following approximation:

$$\delta x_j = x_j - x_0 = x_0 \frac{\mu_j}{\sin^2 \theta_0}, \delta t_j = t_j - t_0 = t_0 \mu_j \frac{\cos 2\theta_0}{\sin^2 \theta_0} \tag{3.3}$$

Here, the unperturbed deflections of the ray path are represented by the values $x_0 = L/\tan\theta_0$ and $t_0 = L/(c_0 \sin\theta_0)$. According to the results (Equation 3.3), both the x-deflection δx_j and the sound speed perturbation μ_j will always have the same sign. That is to say, should μ_j be positive then $\delta\theta_j$ must be negative, which results in the ray having a larger glancing angle and thus a larger δx_j. The opposite also holds true. However, the sign of the time shift is dependent upon both the angle of incidence and the sound speed perturbation. For the case of interest $\theta_0 < 45^o$, the time shift δt_j always holds the same sign as the x-deflection. With $\mu_j > 0$, the path length is longer and the time shift positive. Thus, the sound speed increase is unable to compensate for the increase in path length. The result is an increase in time for the ray to cross the slab. The opposite occurs when $\mu_j < 0$, which means that the ray crosses the slab in less time. That is, for $\theta_0 < 45^o$, changes in the ray path length dominate the scattering of the rays.

A random walk model was tested. First, the sound speed fluctuations μ_n are assumed random, with $\langle \mu_n \rangle = 0$ and $\langle \mu_n \mu_m \rangle = \langle \mu^2 \rangle \delta_{nm}$. Next, Colosi and Flatte (2007) derived the following:

$$dx = \sum_{j=1}^{N} \delta x_j = \frac{x_0}{\sin^2 \theta_0} \sum_{j=1}^{N} \mu_j = \frac{\cos\theta_0}{\sin^3 \theta_0} L \sum_{j=1}^{N} \mu_j \tag{3.4}$$

$$dt = \sum_{j=1}^{N} \delta t_j = t_0 \frac{\cos 2\theta_0}{\sin^2 \theta_0} \sum_{j=1}^{N} \mu_j = \frac{\cos 2\theta_0}{\sin^3 \theta_0} \frac{L}{c_0} \sum_{j=1}^{N} \mu_j \tag{3.5}$$

where dx and dt are the summations of δx_j and δt_j, respectively. Colosi and Flatte (2007) derived the results for the moments of dx and dt.

$$\langle dx^2 \rangle = \left(\frac{\delta x_0}{\sin^2 \theta_0} \right)^2 N \langle \mu^2 \rangle = \frac{\cos^2 \theta_0}{\sin^6 \theta_0} L^2 N \langle \mu^2 \rangle \tag{3.6}$$

$$\left\langle dt^2 \right\rangle = \delta t_0{}^2 \left(\frac{\cos 2\theta_0}{\sin^2 \theta_0} \right)^2 N \left\langle \mu^2 \right\rangle = \frac{\cos^2 2\theta_0}{\sin^6 \theta_0} \frac{L^2}{c_0{}^2} N \left\langle \mu^2 \right\rangle \tag{3.7}$$

The growth of $\left\langle dx^2 \right\rangle$ and $\left\langle dt^2 \right\rangle$ is diffusive because they grow linearly with the number of scattering events (N).

The approximations for δx_j and δt_j were numerically tested with random realizations and sound speeds μ. The following parameter values were chosen: sound speed c_0 = 1500 ms^{-1}, depth of the layer L = 100, number of layers N = 100 and $\left\langle \delta c^2 \right\rangle^{\frac{1}{2}}$ = 0.15 ms^{-1}. The variance of dx and dt were computed for an initial range of angles between 2 and 88 degrees. The approximations proved to be excellent, as demonstrated in Figure 6.

A. DECOMPOSITION ALONG AND ACROSS THE FRONT

The scattered rays need to be compared to the unperturbed wavefront by correcting the scattered ray to the same time as the unperturbed wavefront. With the assumption that the scattered ray propagates at the angle θ_0, Colosi and Flatte (2007) arrived at the following geometrical analysis (see Figure 7):

$$\Delta_W = dx \sin\theta_0, \text{ and } \Delta_R = dx \cos\theta_0 - dtc_0 \tag{3.8}$$

where Δ_W signifies the deviation along the wavefront and Δ_R is the deviation in the ray direction, which is normal to the wavefront. The second term in Δ_R represents the time correction back to the time of the unperturbed front. Through Equation 3.8, a critical understanding of the relative sizes of the two wavefront deviations is achieved. As a result of the fact that dx and dt have the same sign for $\theta_0 < 45^\circ$, the two contributions to Δ_R nearly cancel and the rays fall back along the unperturbed front. As a result of this near cancellation, Δ_R is reduced by a factor of $\tan\theta$ relative to Δ_W. This is a significant result as $\tan\theta$ can be quite small for launch angles near zero degrees. Glancing incidences created a larger distance and thus longer time for crossing the slab, accentuating the effect.

The second moments were then obtained using the random walk model described earlier.

$$\left\langle \Delta_W^2 \right\rangle = N L^2 \left\langle \mu^2 \right\rangle \frac{\cos^2 \theta_0}{\sin^4 \theta_0}, \quad \left\langle \Delta_R^2 \right\rangle = \frac{N L^2 \left\langle \mu^2 \right\rangle}{\sin^2 \theta_0} \tag{3.9}$$

When θ_0 approaches 90 degrees, or near normal incidence, $\cos^2 \theta_0$ approaches zero, thus $\left\langle \Delta_W^2 \right\rangle$ becoming very small; however, $\sin^2 \theta_0$ approaches one, thus $\left\langle \Delta_R^2 \right\rangle$ approaches a constant. As θ_0 approaches zero or glancing incidence, $\left\langle \Delta_W^2 \right\rangle$ grows more rapidly than $\left\langle \Delta_R^2 \right\rangle$ because $\sin^4 \theta_0$ grows more rapidly than $\sin^2 \theta_0$. At θ_0=45 degrees, the curves intersect (see Figure 8). The figure also shows that the Monte-Carlo simulation does very well in approximating $\left\langle \Delta_R^2 \right\rangle$ and $\left\langle \Delta_W^2 \right\rangle$ and is very close to theoretical estimates.

IV. 2-D CONTINUUM MODELS: NO WAVEGUIDE

The discrete 1-D model used in the previous chapter did well to describe the geometry of the problem in question, but, nonetheless, brought forth serious disadvantages. In the 1-D model, the x-component of the ray slowness $\left(\cos\theta/\mathrm{c}\right)$ was a conserved quantity, thus it can strongly affect the fluctuations in the system. From Beron-Vera et al. (2003) and Beron-Vera and Brown (2004), in ray systems in which the sound speed is a function of only one variable. The wave number component perpendicular to the sound speed gradient is constant. When the sound speed varies in multiple directions the wave number components are not conserved and thus, ray chaos can occur (i.e., exponential sensitivity to initial conditions). Further, linearization of the equations was prohibited in the 1-D model at an incident angle of zero as total reflection issues occurred.

A. DEVIATIONS IN THE WAVEFRONT DIRECTION

In the case of no sound channel, the geometry represents an unperturbed ray as a straight line from the source. The direction x is along the unperturbed ray starting at the point (0,0). If there are no fluctuations in sound-speed, the ray arrives at position z = 0 and x = R after time T, as opposed to Z and R+X after time T with fluctuations (see Figure 9). The deviation of Z and X is along the wavefront and perpendicular to it, respectively. Here, Flatte and Colosi (2007) considered an unperturbed ray angle at zero, thus θ will be used to symbolize the angle at position X caused by the perturbations. The perturbation μ is responsible for the deviation in the ray angle and can be estimated from the ray equations. In this way, Colosi and Flatte (2007) calculated the deviation in angle after traveling a distance dx as $\mathrm{d}\theta = -\mu' dx$, where μ' is the random vertical gradient of fractional sound speed. Their equation for the ray angle at Range R is then:

$$\theta\left(\mathrm{R}\right) = \int_0^{\mathrm{R}} \mathrm{d}\theta = -\int_0^{\mathrm{R}} \mathrm{dx}\,\mu'\left(\mathrm{x}\right) \tag{4.4}$$

The integration path of Equation 4.4 is along the path of the unperturbed ray, alongside the x-axis. Thus, after a range R, the variance in the ray angle is:

$$\left\langle \theta^2 \right\rangle = \int_0^R dx_1 \int_0^R dx_2 \left\langle \mu'(x_1)\mu'(x_2) \right\rangle \approx \int_0^R dx \left\langle \mu^2 \right\rangle \frac{L_H}{L_z^2} = \left\langle \mu^2 \right\rangle \frac{L_H R}{L_z^2} \tag{4.5}$$

In evaluating this integral, Colosi and Flatte (2007) made the assumption that the correlation length of the sound speed gradient is short in comparison to the range R in equation 4.5. The correlation lengths of the internal waves along and traverse to the ray are defined as L_H and L_z respectively. Equation 4.5 shows that the rms angle with respect to the horizontal grows as the square root of range.

Now a derivation for the result for the along wavefront scatter is made. Using the supposition that a ray propagates to some position x_1 and undergoes a small angular deflection $\theta(x_1)$, the scattered ray will then propagate to a range R following a straight line and to a depth deflection of $dz(R,x_1)$. Simple geometry (Figure 10) shows that

$$\tan\theta(x_1) \approx \theta(x_1) = \frac{z(x_1)}{R\text{-}x_1}, \text{ or } \frac{\partial z}{\partial \theta}(x_1) = R\text{-}x_1 \tag{4.6}$$

Next Flatte and Colosi (2007) took the sum of all deflections so, the total z-deviation at range R is

$$Z(R) = \int_0^R \frac{\partial z}{\partial \theta}(x_1)\, d\theta = -\int_0^R (R - x_1)\mu' dx_1 . \tag{4.7}$$

The variance of Z is then

$$\left\langle Z^2(R) \right\rangle = R^2 \int_0^R dx_1 \int_0^R dx_2 \left(1\text{-}\frac{x_1}{R}\right)\left(1\text{-}\frac{x_2}{R}\right)\left\langle \mu'(x_1)\mu'(x_2) \right\rangle . \tag{4.8}$$

The two integration variables are within L_H of each other due to a restriction imposed by the correlation function of μ'. Thus, Colosi and Flatte (2007) reduced the integral to the following result:

$$\left\langle Z^2(R) \right\rangle \approx R^2 \int_0^R dx \left(1\text{-}\frac{x_1}{R}\right)^2 \left\langle (\mu')^2 \right\rangle L_H \approx \frac{R^3 \left\langle \mu^2 \right\rangle L_H}{3L_z^2} \tag{4.9}$$

As is evident, rms deviation along the wavefront grows as the 3/2 power of the range.

Numerical evaluations can now be performed for θ_{rms} and Z_{rms} through the estimation of the internal wave factors of Equations 4.5 and 4.9. The following rms values, $\theta_{rms} \approx 6^{\circ}$ and $z_{rms} \approx 60$ km are a result of propagation to a range of 1000 km with sound speed fluctuation values characteristic of internal waves: L_H = 10 km, L_z = 0.1 km, and $\langle \mu^2 \rangle = 10^{-8}$.

B. DEVIATIONS IN THE RAY DIRECTION

The perturbed time δT can be calculated along the ray. X is given by $c_0 \delta T$, where δT is the travel-time deviation for arrival at R calculated along the unperturbed ray. Colosi and Flatte (2007) arrived at the following:

$$X = c_0 T(R) - R = \int_0^R \frac{c_0}{c(x,z)} dx - R \approx \int_0^R \mu(x,z)\, dx \tag{4.10}$$

The variance of X is then:

$$\langle X^2 \rangle = \langle \mu^2 \rangle R L_H \tag{4.11}$$

Comparing rms values, deviation along the wavefront $\langle Z^2 \rangle^{\frac{1}{2}}$ has an rms value of 60 km in contrast to an rms value of only $\langle X^2 \rangle^{\frac{1}{2}}$ = 10 m of the deviation along the ray. This is a surprising result. It says that $\frac{\langle z^2 \rangle^{1/2}}{\langle x^2 \rangle^{1/2}} \approx 1000$, stating that deviation is one-thousand times greater along the front than across it.

C. EXPRESSIONS FOR SOUND PROPAGATION THROUGH INTERNAL WAVES

The wavefront wander τ^2 (Flatté et al., 1979), is directly related to the deviation of the wavefront along the ray $\langle X^2 \rangle$. As such, Colosi and Flatte (2007) derived the following:

$$\left\langle X^2 \right\rangle = c_0^2 \tau^2 = \int_0^R \left\langle \mu^2 (z) \right\rangle L_p (\theta_r = 0, z)\, dx \tag{4.12}$$

where L_p is the correlation length of the internal waves in the x-direction (along the ray) and θ_r is the ray angle with respect to the horizontal. Also, L_p is dependent upon θ_r because internal waves are anisotropic. The deviation in ray angle θ is different in that it is not dependent upon μ, but instead upon the correlation of the vertical gradient of μ. Therefore,

$$\left\langle \theta^2 \right\rangle = \int_0^R \left\langle \mu^2 (z) \right\rangle L_p' (\theta_r = 0, z)\, dx \tag{4.13}$$

where L_p' represents the correlation length of the vertical gradient of the internal waves in the x-direction. Appendix A gives expressions for these correlation lengths. Colosi and Flatte (2007) also show

$$\left\langle Z^2 \right\rangle = R^2 \int_0^R \left(1 - \frac{x}{R}\right)^2 \left\langle \mu^2 (z) \right\rangle L_p' (\theta_r = 0, z)\, dx \tag{4.14}$$

D. NUMERICAL RESULTS

Figure 11 shows the statistics of the rms ray angle and of the rms along the wavefront $\left\langle Z^2 \right\rangle^{\frac{1}{2}}$ and across wavefront $\left\langle X^2 \right\rangle^{\frac{1}{2}}$ deviations. With regards to the range scaling, the rms along the front, plotted in the upper portion of Figure 10, behaves as expected, rapidly growing as $R^{3/2}$. Similarly, the rms ray angle $\left\langle \theta^2 \right\rangle^{\frac{1}{2}}$ displayed in the lower portion of the plot grows as expected by $R^{1/2}$. However, the across the wavefront statistics $\left\langle X^2 \right\rangle^{\frac{1}{2}}$ show some deviation from the prediction of Equation 3.8. Despite the subtraction of the parabolic curve from the Monte-Carlo simulation, at ranges beyond 300 km, the growth rate of $\left\langle X^2 \right\rangle^{\frac{1}{2}}$ ceases to increase by $R^{1/2}$ and jumps to a rate of $R^{3/2}$ for reasons not known (future research). Consequently, a new approach for $\left\langle X^2 \right\rangle^{\frac{1}{2}}$ is required for R>300 km.

E. OCEAN APPLICATIONS: HORIZONTAL PLANE SCATTERING

An important result is obtained when an examination of the horizontal spreading of acoustic rays in the horizontal (lat, long) plane of the previous section is performed. The effect is that this out of plane scattering may now play an important role should the wavefront become obstructed by an island or seamount, which would lead to the healing of the wavefront.

Colosi and Flatte (2007) modified Equation 4.9 to yield the horizontal deviation $\left\langle Y^2 \right\rangle$ for an isotropic sound speed fluctuation field:

$$\left\langle Y^2 \right\rangle = \frac{R^3 \left\langle \mu^2 \right\rangle}{3L_H} \tag{4.15}$$

An order of magnitude can now be obtained using parameters (same as the previous section) typical of ocean internal waves and a propagation range of 1000 km. The rms value of the out of plane deviation $\left\langle Y^2 \right\rangle^{\frac{1}{2}} \approx 600$ m, which shows the effects of internal waves to appear quite small. However, for a random field of mesoscale eddies with $\left\langle \mu^2 \right\rangle \approx 10^{-5}$ and $L_H \approx 50$ km, a much larger rms deviation of 10 km is obtained. Diffraction grows as $R^{1/2}$ as opposed to scattering healing which grows as $R^{3/2}$. That is, diffraction dominates in shorter ranges and scattering healing dominates in larger ranges.

F. WAVEFRONT HEALING IN THE VERTICAL

The following images show the progression of the healing of a wavefront in the vertical past an underwater obstruction with respect to $\left\langle Z^2 \right\rangle^{\frac{1}{2}}$. A sound source emitting rays is considered. Some of the rays will hit the obstruction and others will go over it. As a result, a void or shadow zone will occur with respect to the vertical. As such, the along front scattering in question is demonstrated to reveal faster infilling of the shadow zones than predicted by regular diffraction (not shown). At only 100 km past the obstruction, the wavefront completely fills in the shadow zone.

THIS PAGE INTENTIONALLY LEFT BLANK

V. INCORPORATION OF THE WAVEGUIDE

The results of the no waveguide model were very encouraging, but now we want to treat the important effects of the waveguide. Therefore, it was necessary to modify the theory to incorporate the ocean waveguide and depth dependent ocean internal waves. To better understand this new case a geometrical approach is taken. In the no-waveguide case, the ray propagates to some point x', scatters and then propagates to the final range R. From Snell's law, that ray will shift some vertical differential distance $d\theta$ after traveling some horizontal distance R-x'. As a result, $\frac{dz}{d\theta}$ equals R-x' (see Figure 10). The geometry in the waveguide case is similar to the no-waveguide case except that the ray is now following a curved ray path and not a straight line (Figure 13). Thus, the derivations for the variance in X, Z, and θ remain relatively the same with the exception that $\frac{dz}{d\theta}$ is now dependent upon the ray tube function ζ. Colosi and Flatte (2007) show that

$$\frac{dz}{d\theta}(x') = -\frac{\varsigma_2(x')}{\varsigma_2'(R)} \tag{5.1}$$

The following statistical equations from Colosi and Flatte (2007) are for the waveguide case:

$$\langle X^2 \rangle = \int_0^R ds\, L_p \langle \mu^2 \rangle,\ \langle \theta^2 \rangle = \int_0^R ds\, \langle \mu^2 \rangle L_p',\ \langle Z^2 \rangle = \int_0^R ds\, \langle \mu^2 \rangle L_p \frac{\xi_2^2}{\left(\xi_2^2(R)\right)^2} \tag{5.2}$$

A. NUMERICAL RESULTS

In comparison to the results of the previous chapter, the rms ray angle statistics $\langle \theta^2 \rangle^{\frac{1}{2}}$ continues to show the expected growth of $R^{1/2}$ with some deviation at larger ranges followed by a tapering off at a range of about 1000 km. The across the wavefront statistics $\langle X^2 \rangle^{\frac{1}{2}}$ now grow as $R^{1/2}$ throughout the entire range interval as

opposed to the $R^{3/2}$ seen in the no-waveguide case after 300 km range. Theory fits well for $\left\langle Z^2 \right\rangle^{\frac{1}{2}}$ up to 600 km, but shows deviations at greater range. For large ranges, there maybe a problem with the calculation of the ray tube function ζ past ranges of 600 km. Whereas, the Monte-Carlo simulation tapers off at larger ranges and grows nicely at $R^{3/2}$, the theory shows a dramatic deviation from the model statistics (Figure 14).

VI. CONCLUSIONS

The ray-based physical models did very well in elucidating the physical mechanism for the ocean scattering processes that tend to redistribute acoustic energy dominantly along the wavefront. The models in question do a relatively good job predicting the wavefront distortions caused by the ocean internal waves with respect to Monte-Carlo simulations. For the simple 1-D model, dx and dt have the same sign, thus ray direction variance is diminished. Further, wavefront scattering is dominated by path length changes of the ray. In the continuum models, ray direction deviations depend on μ and grow diffusively as $R^{1/2}$. Also, wavefront direction deviations depend on μ' and there is a moment arm effect that makes $\langle Z^2 \rangle$ grow like $R^{3/2}$. With regards to the waveguide case model, the problem with the theoretical prediction of the Z statistics showing the dramatic deviation with the Monte-Carlo simulation must still be worked out. Nonetheless, the statistics provided for seven degree angle rays propagating through Garrett-Munk internal waves in a Munk sound speed profile remain very compelling, and that the distribution of acoustic energy along the wavefront is dominant.

THIS PAGE INTENTIONALLY LEFT BLANK

VII. FUTURE APPLICATIONS

This paper looked only at one ray with a launch angle of seven degrees using a ray theory approach. This method has some obvious inherent problems. First, a source will emit more than one ray; and, the present ray theory does not give any information concerning the amplitude of the acoustical field. To apply the results presented herein to an operational environment, the energy distribution of all the rays must be inferred by observing where the ray endpoints end up at along the wavefront. Further, the calculations should also be compared with those implementing parabolic equations and normal mode theory to verify results and the effects of diffraction. This new approach will help to understand the practical implications of along the wavefront scattering. One application is the rapid infilling of shadow zones behind underwater obstructions, the significant transfer of acoustical energy from high to low angles, and the dramatic vertical extension of acoustical caustic zones that abut shadow zones that were reported by the Acoustic Thermometry of Ocean Climate group at Navy SOSUS stations in 1999 will be more completely elucidated.

For wavefront healing the important result is the comparison of diffractive healing which scales as $R^{1/2}$ and scattering which scales as $R^{3/2}$. At short ranges, diffraction dominates, but at longer ranges scattering will dominate. Where this transition occurs is unknown.

Further, the theory needs to be compared to experimental data. Because a beam ensonifies only a small group of launch angles, an experiment involving the transmission of a narrow angle beam using an array of sources can meet this need. Littoral Warfare Advanced Development (LWAD) would be an appropriate platform to conduct this experiment.

THIS PAGE INTENTIONALLY LEFT BLANK

APPENDIX A. CORRELATION LENGTHS: THE GARRETT-MUNK SPECTRUM

The GM spectrum is defined by two key variables: vertical mode number j and frequency σ. For every vertical mode, there is some depth they are dependent upon. These depths are in turn locally represented by a harmonic function with a wavenumber given by:

$$k_z = \alpha j N(z) \tag{A.1}$$

$$\alpha = \frac{1}{\pi}\int_0^D dz N(z) \tag{A.2}$$

where D is the ocean depth and N(z) is the buoyancy frequency profile. The following equations are expressions for the correlation length of μ in the direction θ, for the GM model:

$$L_p(\theta, z) = \left\langle j^{-1} \right\rangle \frac{4}{\pi} \frac{1}{\alpha \omega_i} F_1\left(\frac{N(z)\tan\theta}{\omega_i} \right) \tag{A.3}$$

$$\left\langle j^{-1} \right\rangle = M_j \sum_{j=1}^{j_{max}} \frac{1}{j} \frac{1}{j^2 + j_*^2}, \; M_j \left(\sum_{j=1}^{j_{max}} \frac{1}{j^2 + j_*^2} \right)^{-1} \tag{A.4}$$

$$F_1(x) = \left(x^2+1\right)^{-1} + \frac{x^2}{2}\left(x^2+1\right)^{-3/2} \ln \frac{\left(x^2+1\right)^{1/2}+1}{\left(x^2+1\right)^{1/2}-1} \tag{A.5}$$

where j_{max} is a cutoff mode number and ω_i is the inertial frequency. $\left\langle \mu^2 \right\rangle$ and N, the buoyancy frequency, are both functions of depth and j_* is usually equal to three.

The correlation functions for the vertical derivative of μ in the direction θ are obtained by giving

$$L_p'(\theta, z) = (\alpha N)^2 \langle j \rangle \frac{4}{\pi} \frac{1}{\alpha \omega_i} F_1\left(\frac{N(z)\theta}{\omega_i} \right) \tag{A.6}$$

$$\langle j \rangle = M_j \sum_{j=1}^{j_{max}} j \frac{1}{j^2 + j_*^2} \tag{A.7}$$

The cutoff mode number j_{max} is of importance for L_p' given the divergence of $\langle j \rangle$ for $j_{max} \to \infty$. Through observation, j_{max} is established when the vertical wavenumber of the internal waves equals 0.1 cpm (Duda et al 1992).

APPENDIX B FIGURES

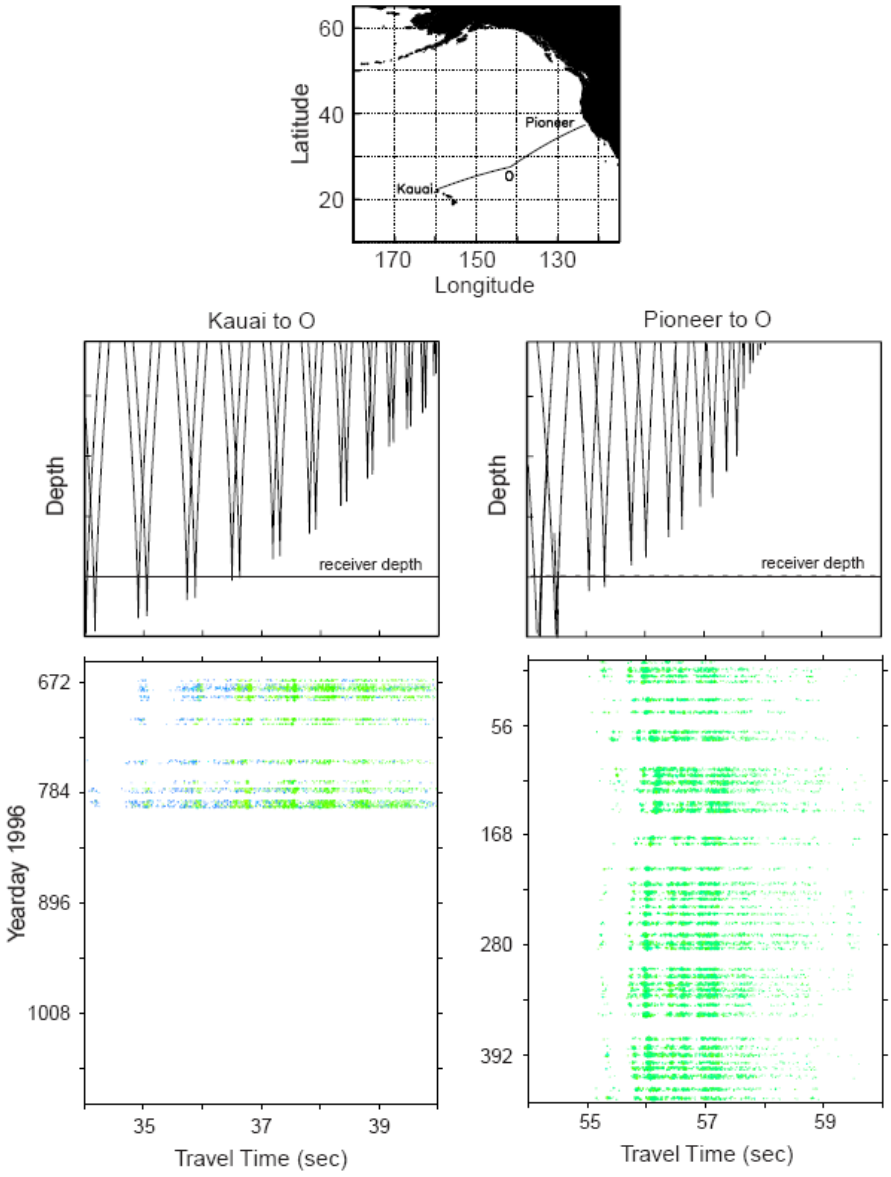

Figure 1. Wavefront data collected from Navy SOSUS receivers.

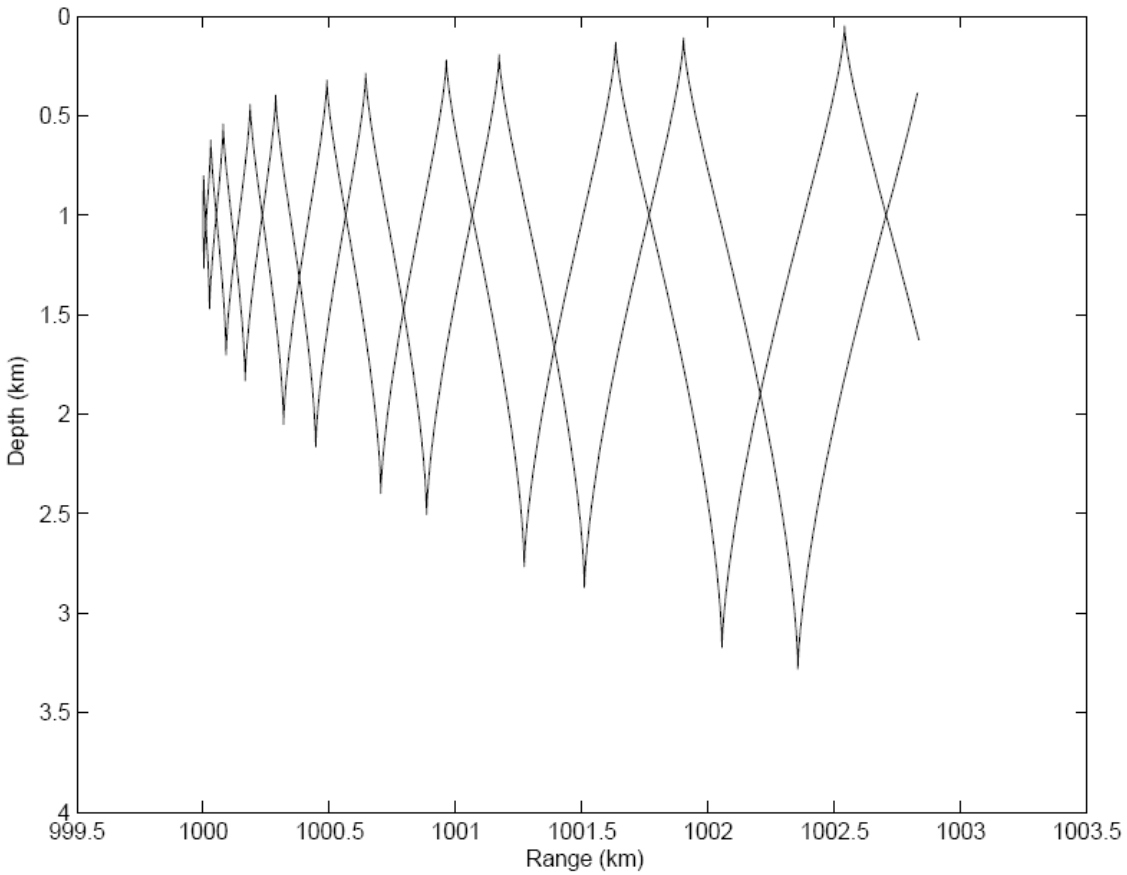

Figure 2. A ray computation showing an acoustic wavefront at roughly 1,000-km range, resulting from a point source on the sound channel axis. The calculation was carried out using a Munk canonical sound-speed profile without internal-wave sound-speed perturbations.

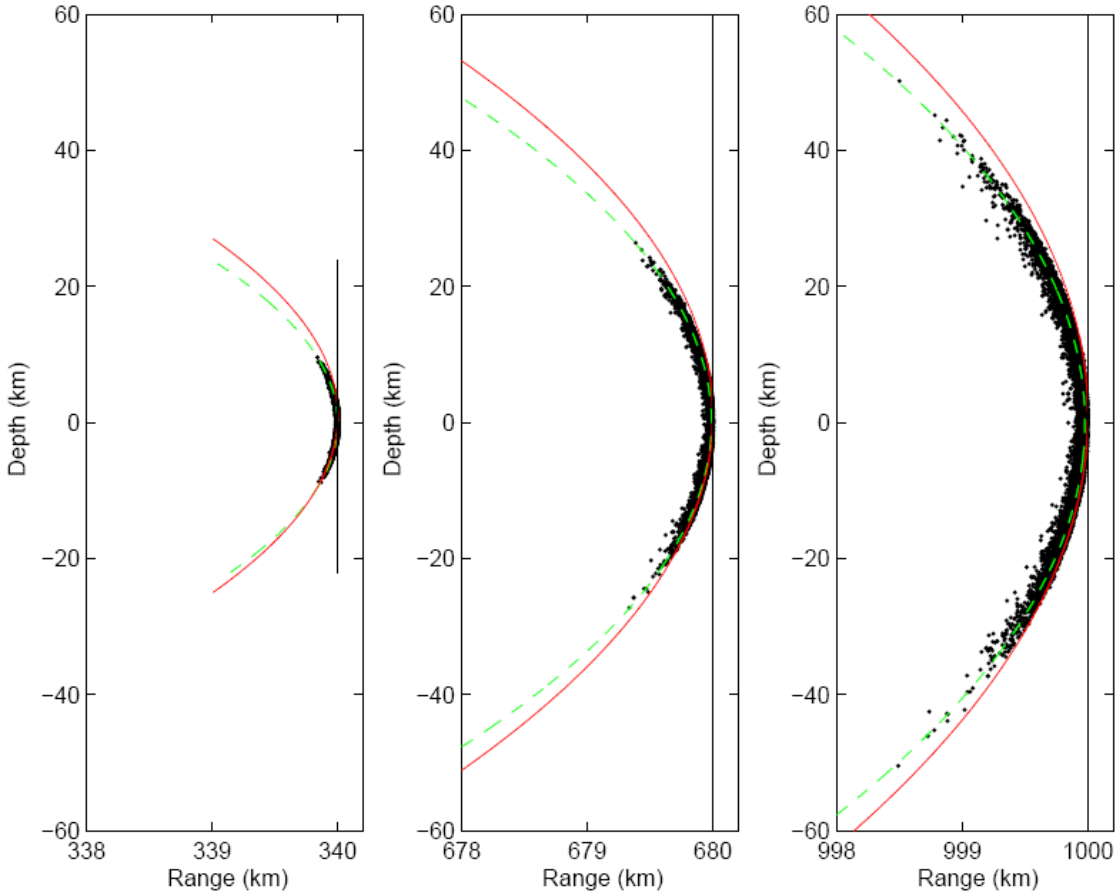

Figure 3. Range evolution of the ray endpoints for 12,000 realizations of ray propagation through internal wave induced sound speed perturbations. For all realizations the initial angle is zero degrees and the initial depth is 1,000 m. The solid vertical lines show the location of the unperturbed wavefront, assumed a plane wave. The dash red curve shows a parabolic fit to the ray endpoint distributions, and the green curve shows the location of the unperturbed point source front.

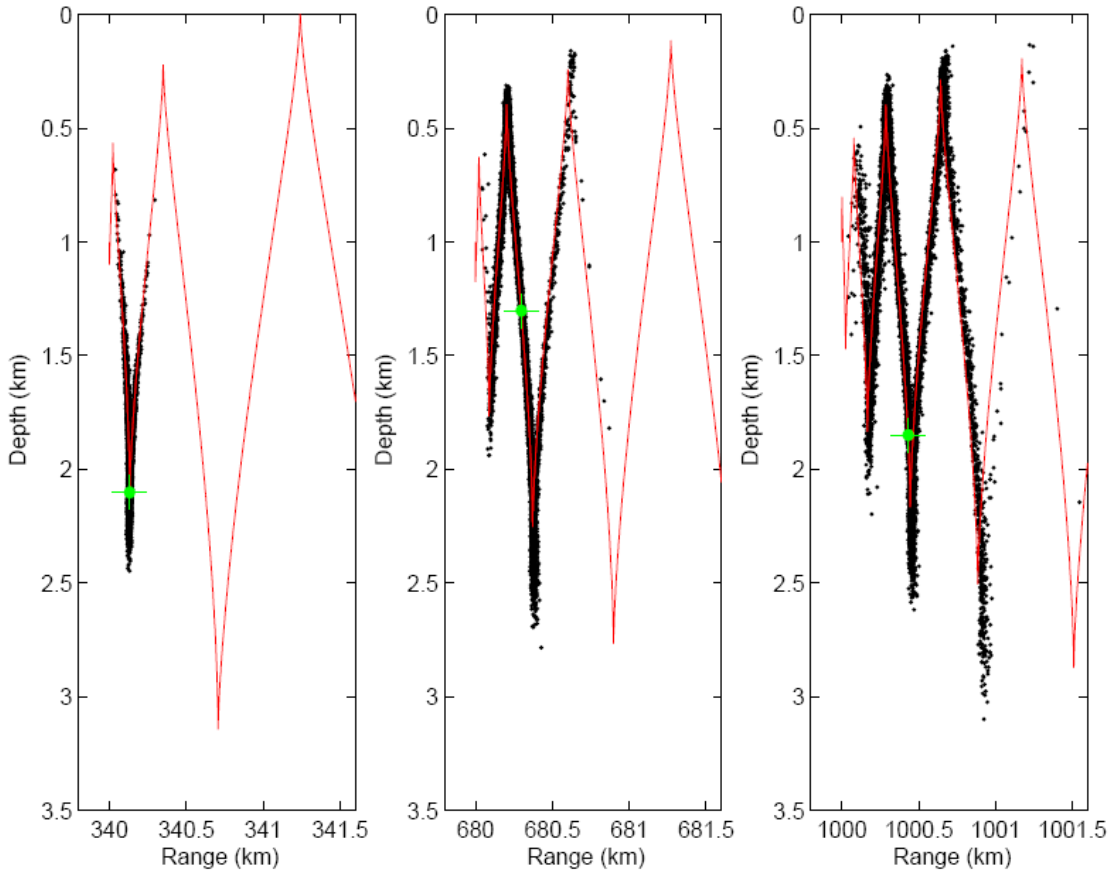

Figure 4. Range evolution of the ray endpoints for 12,000 realizations of ray propagation through internal wave induced sound speed perturbations, with the Munk canonical profile. For all realizations the initial angle is 7 degrees and the initial depth is 1000-m. The red curve shows the unperturbed wavefront from a point source, and the green dot shows the location of the unperturbed 7 degree ray.

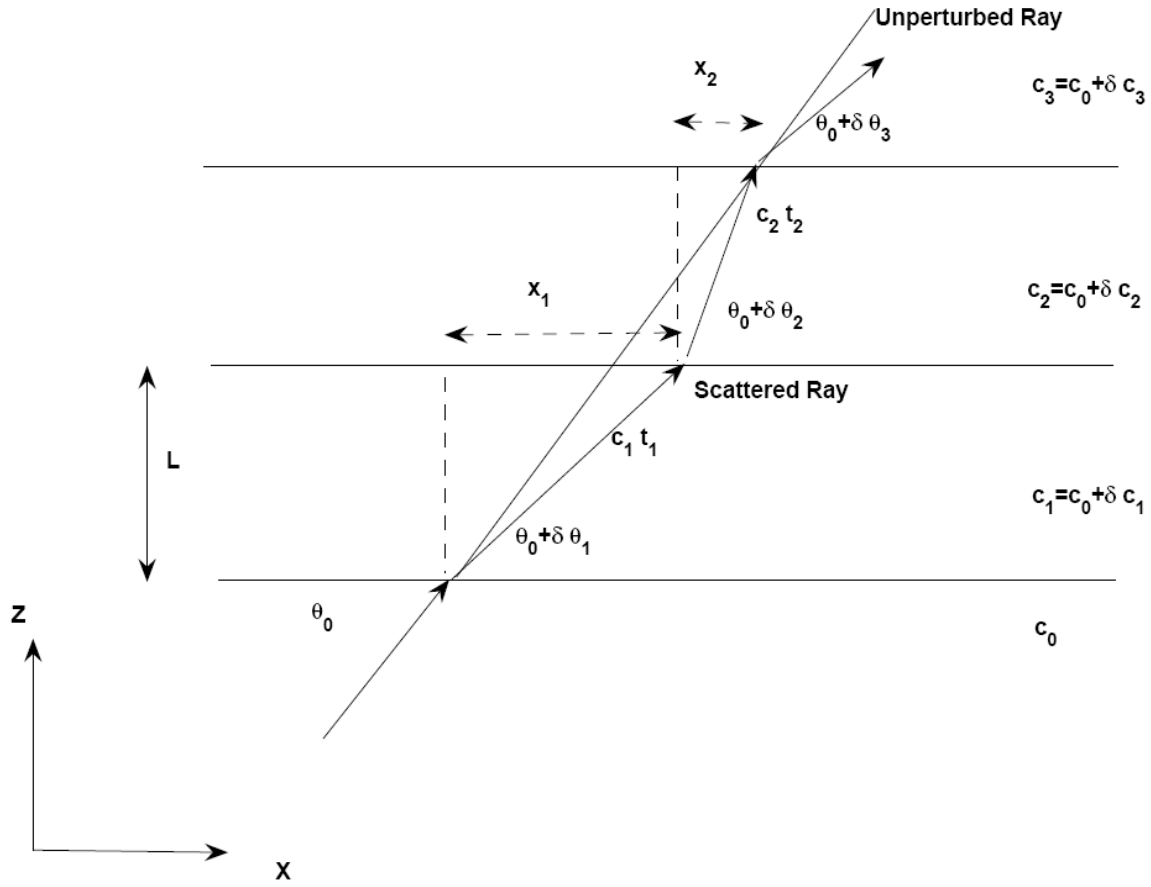

Figure 5. Schematic showing the geometry of the 1-dimensional discrete layer problem.

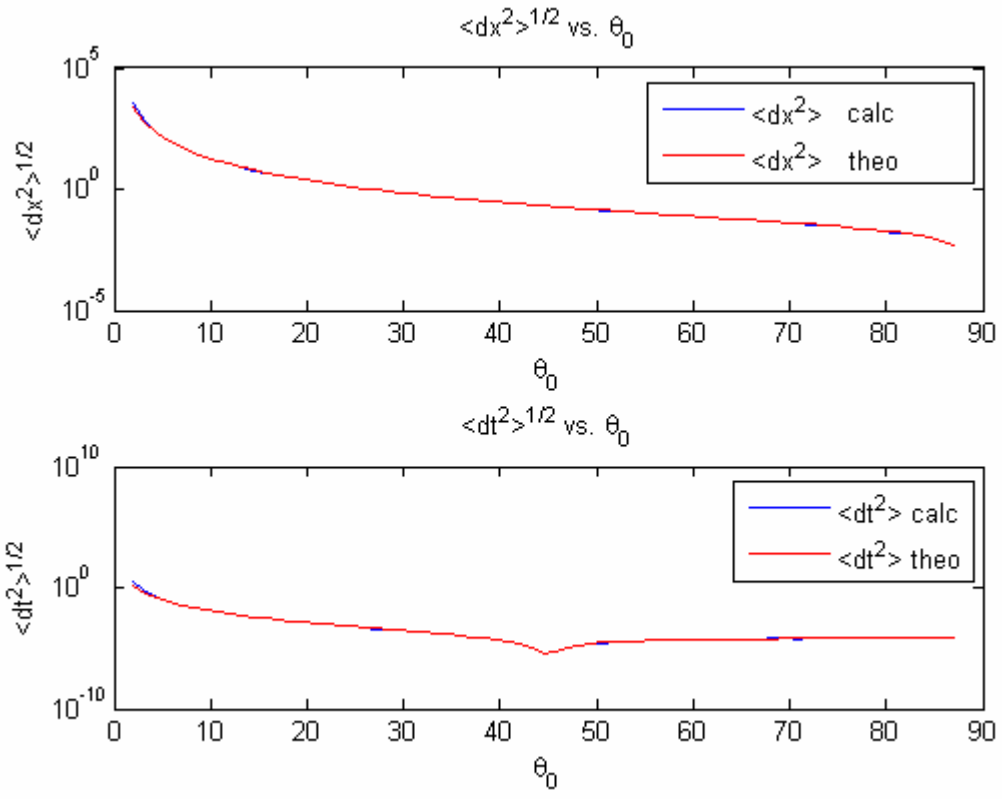

Figure 6. Comparison of statistics for dx and dt as a function of the initial angle θ_0, using the random walk model. The blue curves represent the Monte Carlo simulations and the red curves are the theoretical estimations.

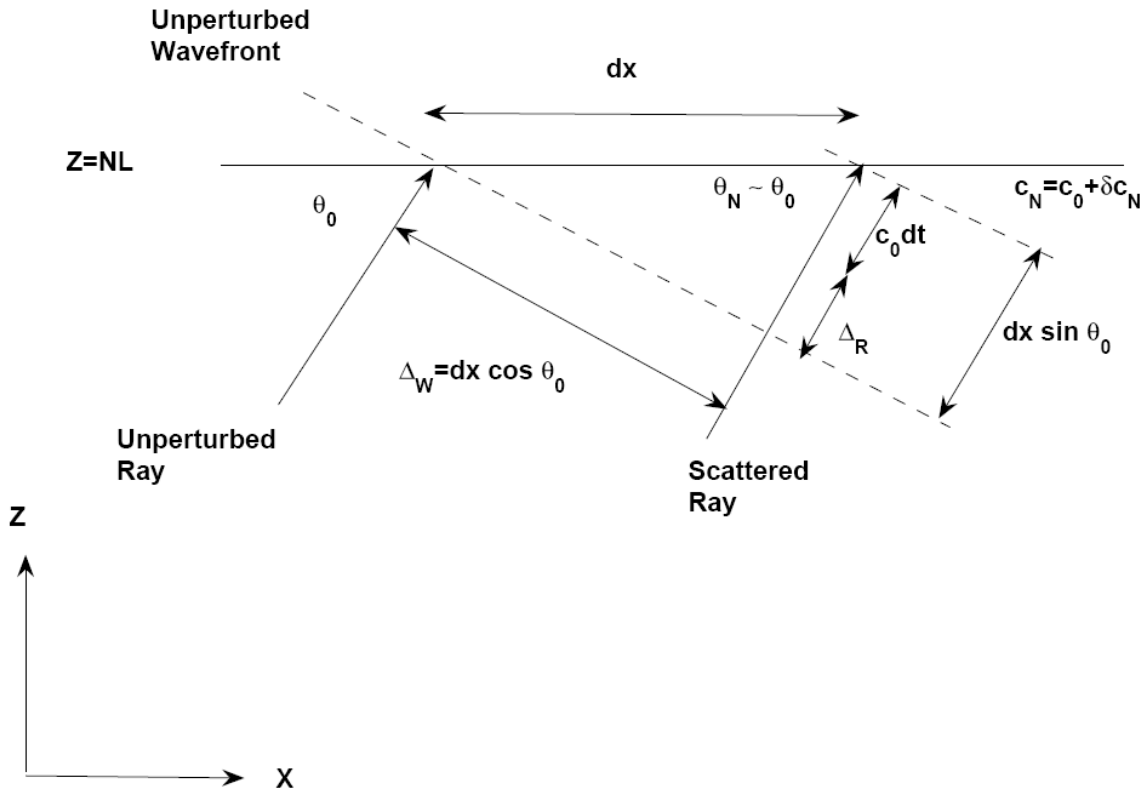

Figure 7. Schematic of the geometry of the projection of the scattered ray onto the unperturbed wavefront.

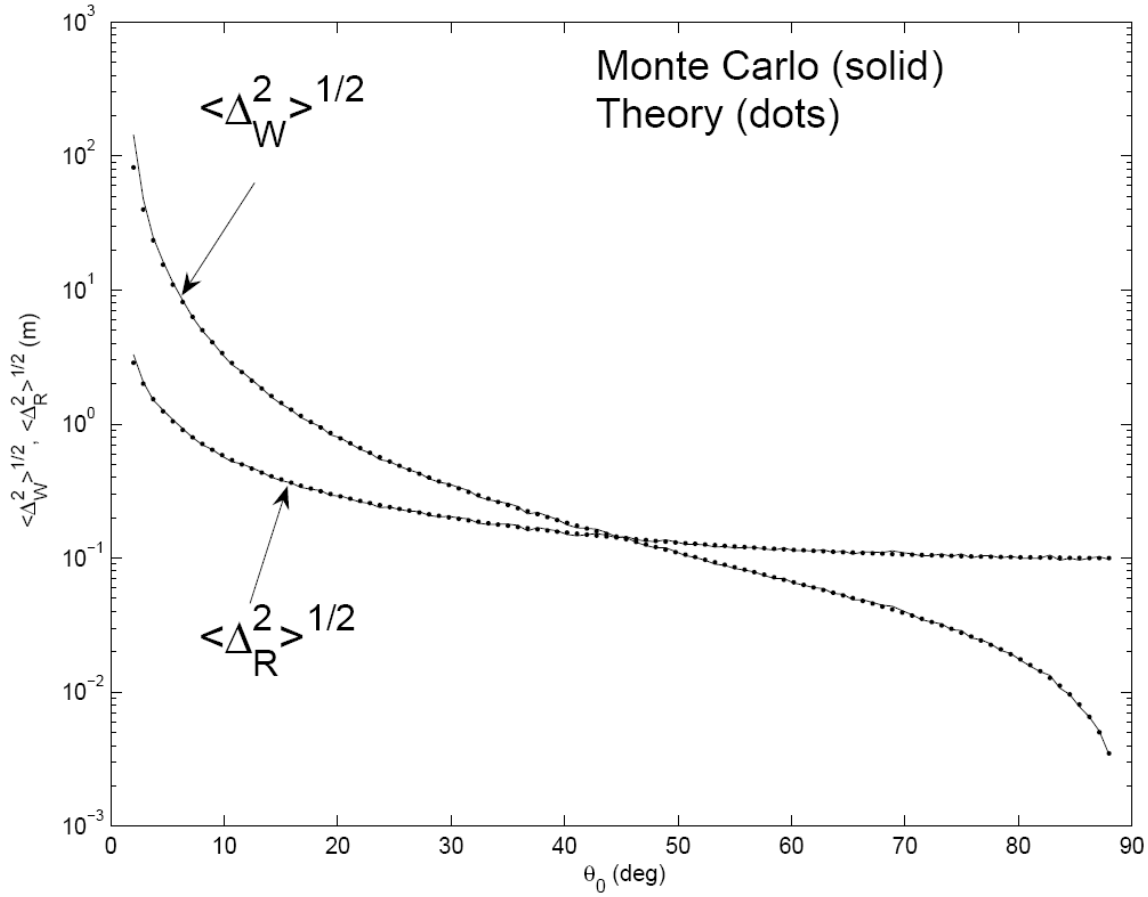

Figure 8. Computations of $\langle \Delta w^2 \rangle$ and $\langle \Delta R^2 \rangle$ as a function of initial θ_0, from direct Monte-Carlo numerical simulation and from theoretical estimates using Eq. 3.9.

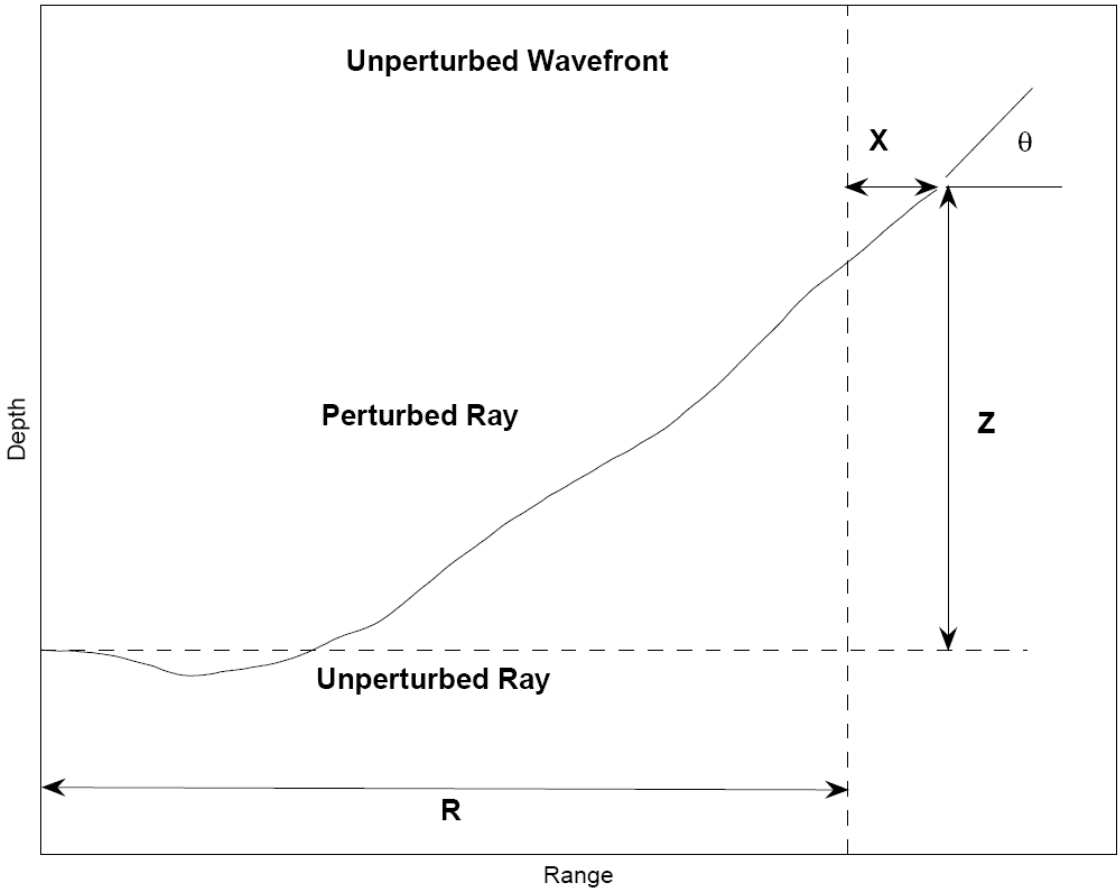

Figure 9. Geometry of ray scattering in the absence of a waveguide.

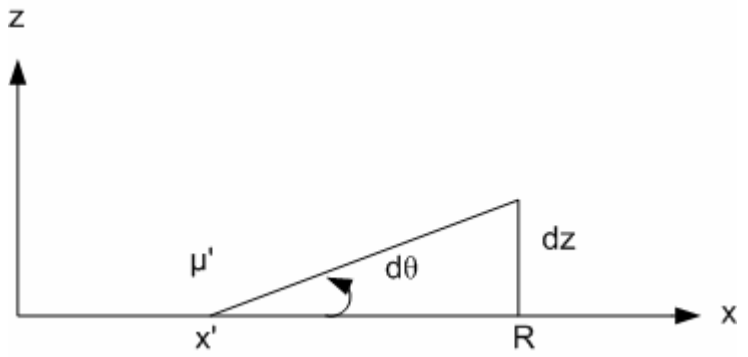

Figure 10. Geometrical description of the application of Snell's Law to the no-waveguide case.

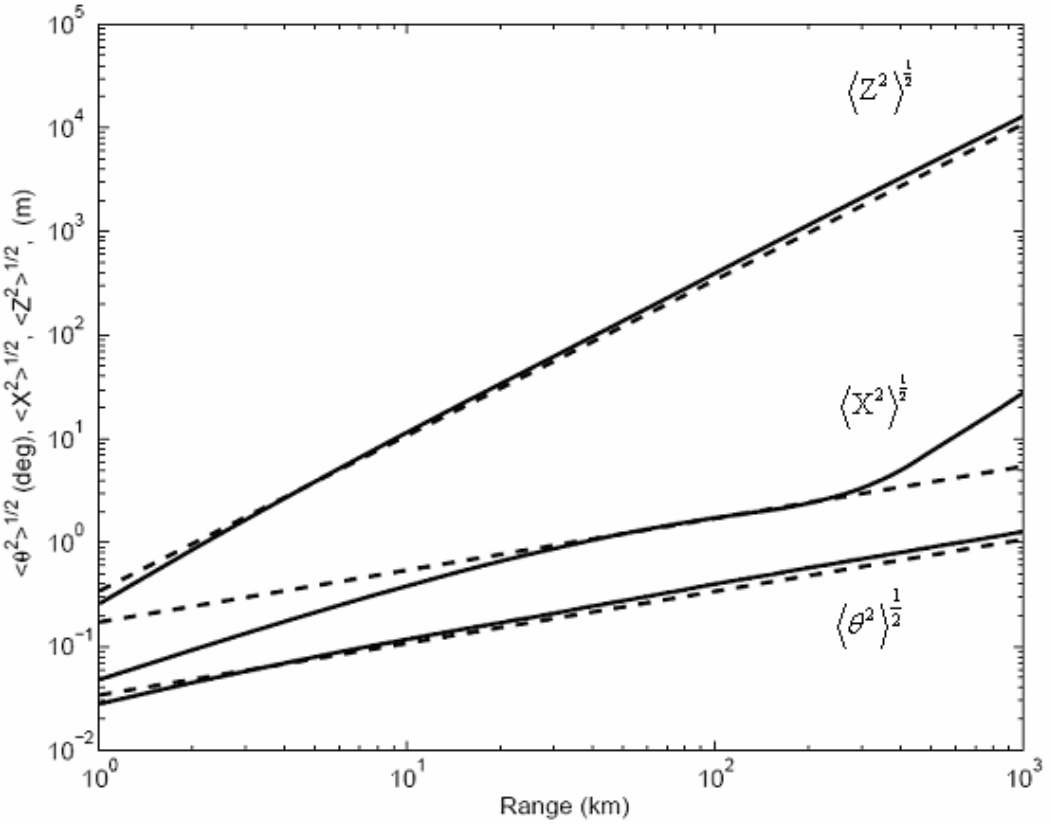

Figure 11. Computations of rms ray deflections for zero angle rays propagating through GM internal waves (solid) and theoretical expectations (dash). The rms angle is diplayed in the lower portion of the plot, showing the expected growth by $R^{1/2}$. The rms along the wavefront deflection is diplayed in the upper portion of the plot, also showing the expected $R^{3/2}$ growth. The ray direction deflection is displayed in the middle section of the plot where the numerical result has been corrected for the parabolic spreading of the ray endpoints. The $R^{1/2}$ scaling breaks down after 300-km in range.

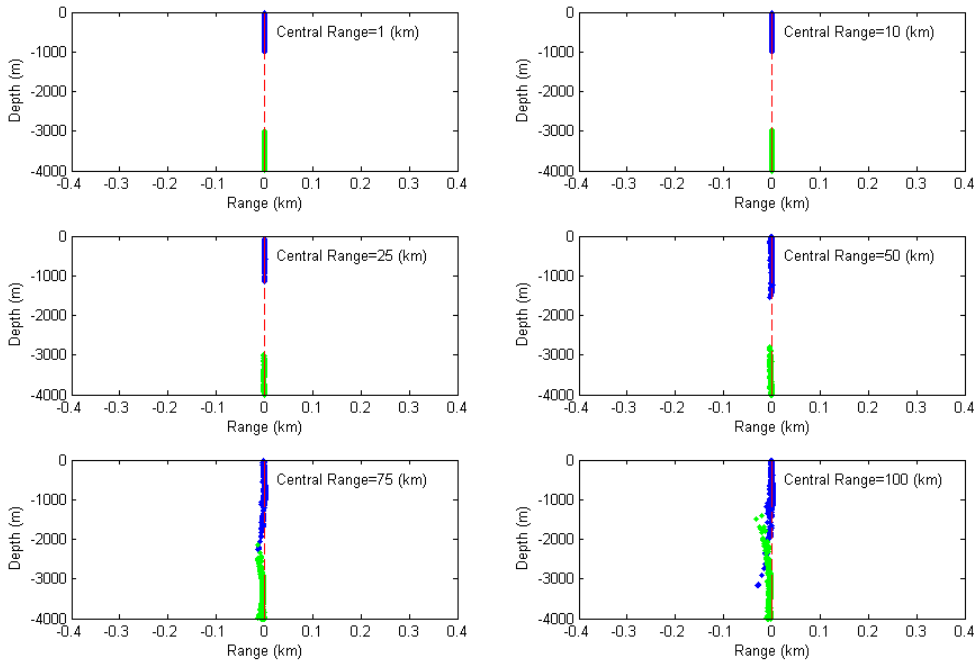

Figure 12. Progression of along the wavefront scattering past an underwater obstruction demonstrating a complete infilling of the shadow zone at a range of 100 km.

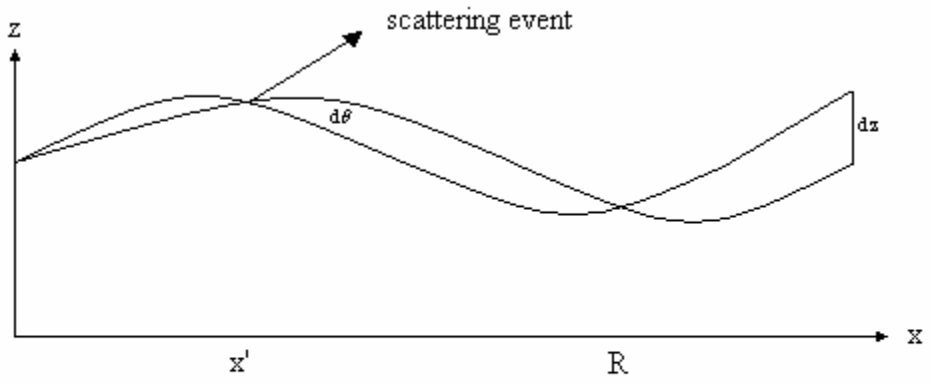

Figure 13. Geometrical description of the application of Snell's Law to the waveguide case.

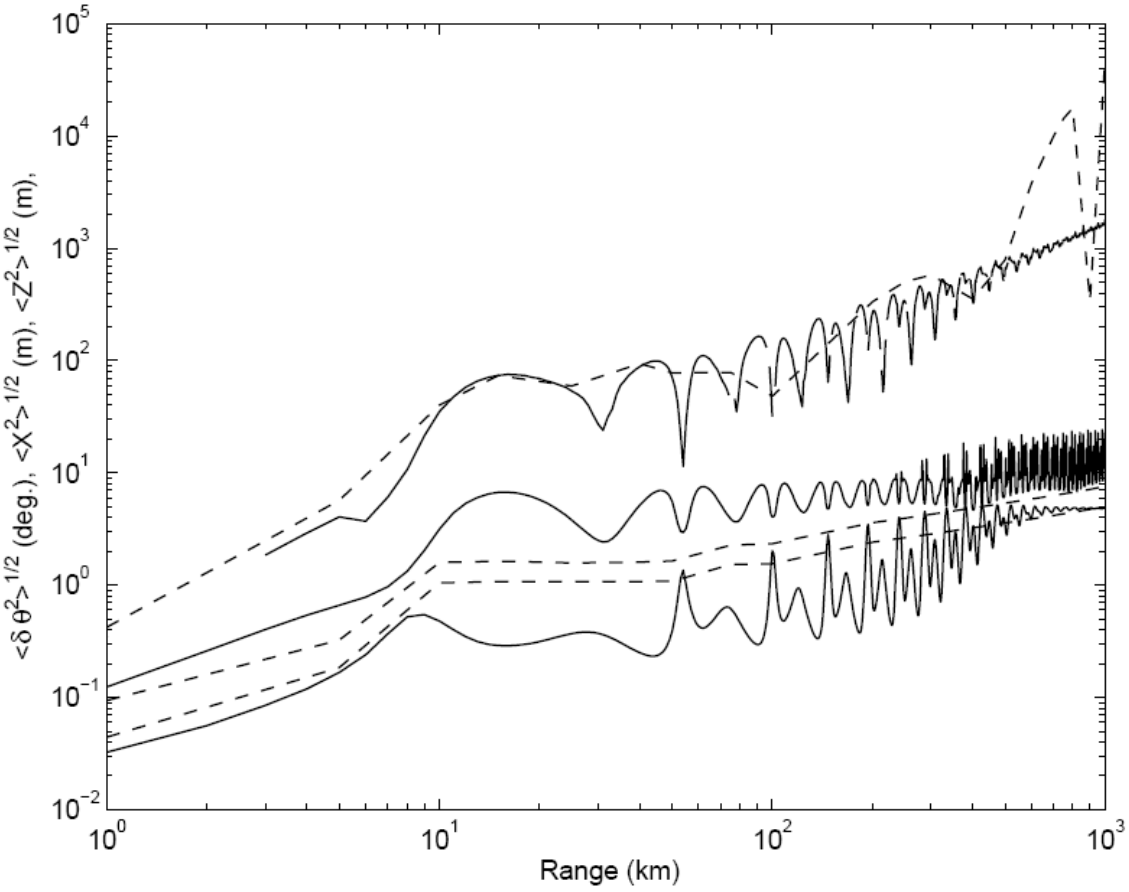

Figure 14. Computations of rms ray deflections for 7 degree angle rays propagatingthrough GM internal waves in a Munk sound speed profile. Monte-Carlo simulation results are shown with solid lines while theoretical results are dashed. The rms ray angle is in the lower portion of the plot and the expected display of $R^{1/2}$ is evident. The rms along wavefront deflection is displayed in the upper portion and the expected growth of R3/2 is evident. The rms across the wavefront is in the middle of the plot and shows the expected growth of $R^{1/2}$.

LIST OF REFERENCES

Beron-Vera, F. J., M. G. Brown, J. A. Colosi, S. Tomsovic, A. L. Virovlyansky, M. Wolfson, and G. M. Zaslavsky (**2003**). "Ray dynamics in a long range acoustic propagation experiment," J. Acoust. Soc. Am. V114(3), 1226-1242.

Beron-Vera, F.J., and M. G. Brown (**2004**). "Travel time stability in weakly range-dependent sound channels," J. Acoust. Soc. Am. 115, 1068-1077.

Brown, M.G., J.A. Colosi, S. Tomsovic, A.L Virovlyansky, M.A. Wolfson and G.M. Zaslavsky (2003). "Ray dynamics in long range deep ocean sound propagation," J. Acoust. Soc. Am. V113, 2533-2547.

Colosi J.A. and M.G. Brown (1998). "Efficient numerical simulation of stochastic internal-wave-induced sound-speed perturbation fields," J. Acoust. Soc. Am. 103, 2232-2235.

Colosi J.A., and S.M. Flatte (2007). "Anisotropy of the wavefront distortion for acoustic pulse propagation through ocean sound-speed fluctuations: A ray perspective (article in progress).

Dushaw, B.D., B.M. Howe, J.A. Mercer, and R.C. Spindel (1999). "Multi-megameter range acoustic data obtained by bottom mounted hydrophone arrays for measurement of ocean temperature," IEEE J. Oceanic Eng. 24(2), 203-215.

Duda, T.F., S.M. Flatte, J.A. Colosi, B.D. Cornuelle, J.A. Hildebrand, W.S. Hodgkiss, P.F. Worcester, B.M. Howe, J.A. Mercer, and R.C. Spindel (1992). "Measured wavefront fluctuations in 1000-km pulse propagation in the Pacific Ocean," J. Acoust. Soc. Am., V92(2), 939-955.

Flatte S.M., R. Dashen, W. Munk, K. Watson and F. Zachariasen (1979). *Sound Transmission through a Fluctuating Ocean* (Cambridge University Press, Cambridge).

Munk, W. (1974). "Sound channel in an exponentially stratified ocean, with application to SOFAR," J. Acoust. Soc. Am., V55(2), 220-226.

THIS PAGE INTENTIONALLY LEFT BLANK

INITIAL DISTRIBUTION LIST

1. Defense Technical Information Center
   Ft. Belvoir, Virginia

2. Dudley Knox Library
   Naval Postgraduate School
   Monterey, California

3. Dr. John A. Colosi
   Naval Postgraduate School
   Monterey, California

4. CDR D. Benjamin Reeder
   Naval Postgraduate School
   Monterey, California

5. Dr. Mary L. Batteen
   Naval Postgraduate School
   Monterey, California

6. Maxsimo Salazar
   Naval Postgraduate School
   Monterey, California